powders

MDPI

Article

Size Classification and Material Sorting of Fine Powders with a Deflector Wheel Air Classifier and an Electrostatic Separator

Mohamed Abohelwa [1,*], Annett Wollmann [1], Bernd Benker [2], Alexander Plack [1], Mehran Javadi [1] and Alfred P. Weber [1]

[1] Institute of Particle Technology, Clausthal University of Technology, 38678 Clausthal-Zellerfeld, Germany; annett.wollmann@tu-clausthal.de (A.W.); alexander.plack@tu-clausthal.de (A.P.); mehran.javadi@tu-clausthal.de (M.J.); weber@mvt.tu-clausthal.de (A.P.W.)

[2] CUTEC Forschungszentrum, 38678 Clausthal-Zellerfeld, Germany; bernd.benker@cutec.de

* Correspondence: ma96@tu-clausthal.de

Abstract: In this study, a two-dimensional separation of microparticles based on their settling velocity and triboelectric charge ability is achieved using an air classifier for size fractionation and simultaneous charging, followed by an electrostatic separator. In the first part, considerations for enhancing particle classification with high sharpness and low-pressure drops are discussed through improvements in blade design investigated with CFD simulations and validated experimentally. Blades with extended lengths towards the center of the classifier prevent the formation of high-velocity vortices, thereby minimizing the back-mixing of particles and enhancing separation sharpness. This approach also reduces pressure drops associated with these flow vortices. In the second part of the study, the modified blades within the classifier are utilized for two-dimensional separation. Powders from two different materials are fed into the classification system, where particles become triboelectrically charged, mainly through collisions with the walls of the classification system components. Coarse particles are rejected at the wheel and exit the classifier, while differently charged fine particles of the two materials are directed into an electrostatic separator for material sorting. An enrichment of approximately 25–35% for both materials has been achieved on the electrodes of the separator.

Keywords: deflector wheel classifier; fine powders; CFD; cut size; separation sharpness; triboelectric charging; electrostatic separation

Citation: Abohelwa, M.; Wollmann, A.; Benker, B.; Plack, A.; Javadi, M.; Weber, A.P. Size Classification and Material Sorting of Fine Powders with a Deflector Wheel Air Classifier and an Electrostatic Separator. *Powders* **2024**, *3*, 550–573. https://doi.org/10.3390/powders3040029

Academic Editor: Paul F. Luckham

Received: 16 September 2024
Revised: 5 November 2024
Accepted: 8 November 2024
Published: 12 November 2024

1. Introduction

The German Science Foundation funded the priority program SPP 2045, entitled "MehrDimPart—highly specific multidimensional fractionation of technical fine particle systems", in 2016. The program's objective is to develop processes for the multidimensional fractionation of particles smaller than 10 µm, enabling the precise control over particle properties while significantly increasing production throughput. As a part of the SPP 2045 program, this study represents a process for the two-dimensional separation of fine particles based on their size with simultaneous material sorting.

Particulate intermediate products form the basis for the vast majority of high-quality industrial products, including ceramic and powder metallurgical components, coatings, porous functional structures, printed electronics, etc. [1,2]. There is enormous potential for highly specified particle systems, especially in the size range < 10 µm. In order to fully leverage this potential, it is often necessary to fractionate the powders according to several particle characteristics [3].

In many technically relevant fields, separating particles smaller than 10 µm based on size or other properties is a persistent challenge [4]. In particular, the separation and sorting of micron-sized particles is crucial for environmental assessment, food and chemical processing, biological and chemical analyses, and diagnostics [5].

In contrast to wet processes, dry sorting processes are characterized by a high throughput, continuous processes, and the complete elimination of chemical additives and complex drying steps [6]. While simple dry sorting processes based on triboelectric charging have been implemented in the size range of several 10 µm [7,8], dry material-specific separation in the range of a few micrometers down to the submicron size range is still pending.

The deflector wheel classifier has established itself industrially in dry powder classification in the ultra-fine range (refer to Section 2 for the working principle of the classifier). Air classifiers are widely recognized for their efficacy in segregating dry powders into distinct size categories [9,10]. Industrially, they are used in combination with mills or as classifier mills [11]. Moreover, classifiers can be integrated with material sorting techniques to achieve multi-dimensional separation.

Spötter [12] conducted Faraday cup electrometer measurements after a deflector wheel classifier to assess the charge acquired by particles following classification. The tests showed that material-specific charging also occurs when ultrafine powders pass through. Spötter also investigated the charging behavior of various materials with particle sizes in the range of several micrometers using a dry disperser (RODOS® from Sympatec Inc., Clausthal-Zellerfeld, Germany). The RODOS® system operates based on the injector concept, where material in the form of particle agglomerates is introduced into the system, mixed with air, and accelerated through a free jet [13]. The study revealed that different materials can exhibit different polarities and magnitudes of charge. The charging of fine particles in the micron to submicron size range has been studied in [13], where particles have been charged through collisions with the walls of a RODOS-disperser (RODOS® from Sympatec Inc., Clausthal-Zellerfeld - Germany) under varying operating conditions. The tests in [13] have shown that particles in this size range also acquire charges with different polarities through contact with the disperser walls. In the current study, the RODOS-disperser used in [13] is coupled with an air classifier and an electrostatic separator, as shown in Figure 1. Therefore, the study aims to clarify whether this charging is sufficient for sorting ultra-fine powders by material in a downstream electrostatic separator in addition to aerodynamic classification, thus realizing a two-dimensional separation of particles in this size range with applications in powder recycling.

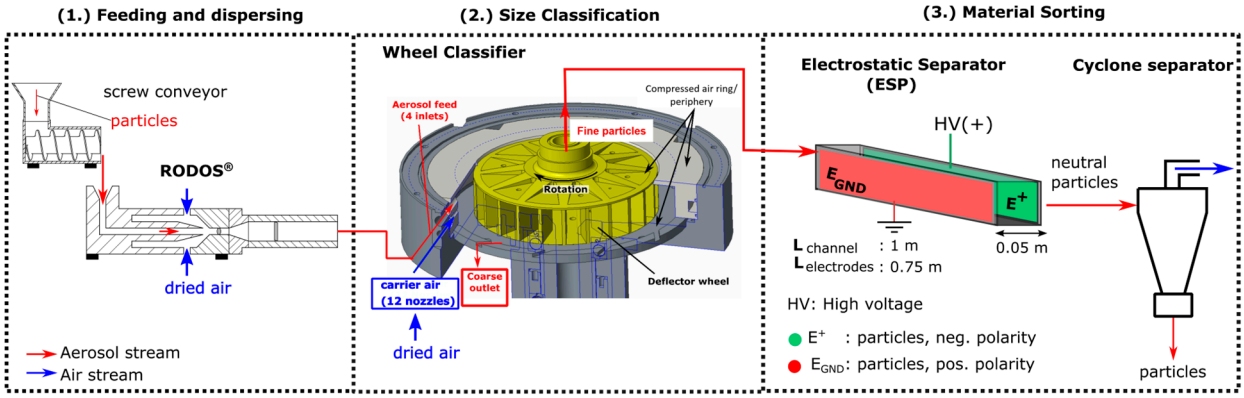

Figure 1. Overview of the whole classification system coupled with the material sorting system. The wheel classifier in (2.) is equipped with 12 airflow and 4 particle inlet nozzles evenly distributed around the circumference (wheel diameter: 200 mm, gap between wheel and casing: 25 mm, wheel height: 40 mm). The Figure of the wheel classifier is adapted from [14].

The collisions of particles with the high-speed rotating blades of the classifier are utilized to induce tribocharging, which is crucial for the material sorting process. When applying condenser or charge relaxation models [15] or a Hertzian contact model [16], tribocharging can be influenced by various factors and parameters, which may, in turn, be affected by the classifier's operational parameters. These factors include the frequency and number of particle–wall collisions, the speed of collision, the duration of contact, and the

contact area. Additionally, particle–particle collisions may also impact the tribocharging process, which can be influenced by changes in the classifier's operating parameters. Variations in the classifier's operating parameters, such as the blades' rotational speed or the volume flow rate, can significantly impact the separation cut size. Consequently, the mass-loading of non-separated particles that reach the blades' region (fine material) may vary. In [17] by Watano, it was observed that an increase in particle mass loading led to a reduced net charge during pneumatic conveying for the mass-specific charging of PMMA particles. Numerical simulations of particle movement in [17] suggested that as loading increases, the frequency of interparticle collisions rises more sharply than particle–wall collisions. Additionally, the study noted that an increase in particle velocity contributed to a higher net charge on the particles.

In addition to the direct effect of particle velocity on the acquired charge, velocity can also influence the contact area, which is another critical factor in charge acquisition. Studies [18,19] observed a linear relationship between the vertical impact velocity and the contact area for PMMA and Nylon particles, respectively [14]. The contact area can further affect the contact angle, and together with contact speed, these parameters influence the duration of contact [14,16]. Regarding the number of collisions, it was concluded in [15] that the charge acquired by a single particle can be increased by raising the number of collisions or extending the length of the contact surface. Therefore, variations in the classifier operating parameters are conducted to gain an understanding of the particle tribocharging in air classifiers during a two-dimensional separation process.

For efficient two-dimensional separation, optimizing the aerodynamic separation process is paramount. This optimization entails enhancing separation sharpness to obtain fine materials with a narrow particle size distribution while excluding undesired coarse materials. Additionally, reducing the loss of fine materials misclassified as coarse further refines the process by increasing the amount of material to be sorted. As two-dimensional separation involves an additional apparatus (electrostatic separator, Figure 1), minimizing pressure losses is also essential to maintain flow and energy efficiency. These optimizations collectively ensure that the overall process is effective, sustainable, and realizable. Classifying fine powders presents challenges and limitations that can compromise separation sharpness. In [20], these limitations were discussed, highlighting instances where high rotational speeds of the classifier and low flow rates may unexpectedly fail to reduce the cut size of separation (x_{50}). Instead, they may lead to a reduction in separation sharpness, contrary to theoretical expectations. Therefore, the first part of this study involved conducting CFD simulations and experimental investigations conducted by the same authors, focusing on enhancing the sharpness of the cut and reducing pressure drops. This was achieved through modifications in blade geometry, with a particular focus on extending the blade length toward the center of the classifier.

As shown schematically in Figures 1 and 2, a deflection wheel classifier can be segmented into three distinct regions [11,21]. Notably, one of these regions encompasses the space between the outlet of the classifier blades and the center of the classifier (region from r_i to the center in Figure 2a,b. This particular region has not received significant attention in air classifier research. Instead, the focus has predominantly been on optimizing the separation process through adjustments to the operating parameters [22–25] or modifications of the classifier's stationary blades (guide vanes) [9,26–28] or the rotating blades [29–31]. Liu et al. [27] coupled guide blades into the classifier and discovered that inclined guide blades effectively stabilized the flow field, resulting in improved classification efficiency compared to the original non-inclined guide blades. Yu et al. [28] presented a guide vane design method based on particular airflow trajectories under specified operating conditions. Their logarithmic spiral guide blades achieved similar separation results for particles of the same size as the original blades, effectively altering the non-uniform circumferential flow field distribution in the annular region. Zeng et al. [9] proposed the following three new configurations for turbo air classifier guide vanes: direct-type, L-type, and logarithmic spiral type, as well as a setup without guide vanes. Guide vanes improved flow field

stability compared to those without them. Logarithmic guide vanes outperformed other designs by improving separation sharpness and reducing cut size. Mou et al. [32] compared the effectiveness of streamlined (curved) blades, designed using the single arc method, to conventional straight blades. The study found that curved blades improved flow distribution, resulting in a 5% reduction in cut size, while maintaining separation sharpness. Ren et al. [30] used non-radial arc blades in a rotor cage to reduce vortex formation and improve flow distribution. This modification improved separation efficiency, resulting in a fine powder with a controlled particle size distribution, compared to straight blades. Zhao et al. [31] investigated the effects of blade geometry on air classifier performance. The researchers found that using positively bowed blades with a low impact angle effectively eliminated the flow vortex in the classifier. Furthermore, these positively bowed blades improved the classification process, generating fine powders with a narrow particle size distribution, compared to straight blades.

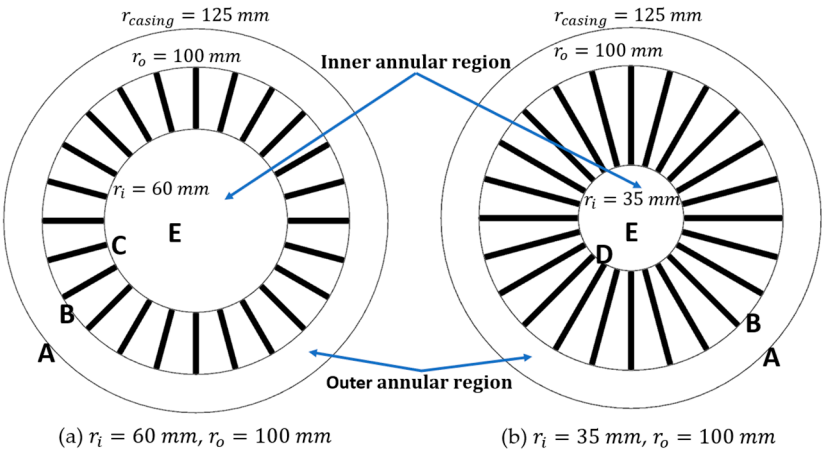

Figure 2. Blades with different inner radii.

The inner annular region garnered interest in [10], where flow baffles were incorporated to reduce the pressure drop throughout the classifier by disrupting vortex formation within that space. Additionally, ref. [33] delved into examining the impact of the blades' inner and outer diameters on the flow field and the classification process. By adjusting the two diameters while maintaining consistent blade length, alterations in the size of the two annular regions before and after the blades can be achieved. The closer placement of the blades to the center of the classifier has been observed to result in a slight increase in separation sharpness.

While previous studies, such as [10,33], focused on geometric modifications to the annular region surrounding the center of the classifier, the impact of this region on the classification process was overlooked. In these studies, classification was assumed to occur primarily in the outer annular region, before the blades or between the classifier blades. However, the current study reveals a significant effect of this central region on the classification process. The formation of flow vortices with higher flow tangential velocities in the inner annular region may induce an additional classification zone, which could become dominant at higher rotational speeds or low flow rates, as demonstrated in [20]. In that study, the cut size at high rotational speeds and low flow rates was closer to the theoretical cut size calculated at the inner radius of the blades using Equation (1), refs. [10,34]. This equation results from the equilibrium of the two forces that act on the particles, namely drag and centrifugal forces, with the assumption that the particle motion falls within the Stokes range [35]. In Equation (1), v_r represents the radial velocity of the flow, v_ϕ denotes the circumferential velocity of the flow, η stands for the dynamic viscosity

of the air, ρ_p is the density of the particle, and r is the radius of the classifier, typically where the theoretical cut size is calculated and the classification is expected to occur.

$$x_{50,th} = \sqrt{\frac{18 \cdot v_r \cdot r \cdot \eta}{v_\phi^2 \cdot \rho_p}} \quad (1)$$

Extending the blades' length toward the center would mitigate the effect of the flow vortices, formed in the inner annular region, on the classification process, maintaining relatively high separation sharpness even at high rotational speeds.

To evaluate the classification process, the separation efficiency, T(x), is plotted against the particle diameter in the separation curve, also known as the tromp curve. The separation efficiency, T(x), is derived from Equation (2) and denotes the proportion of feed material that remains in the coarse material fraction following the separation process. In Equation (2), the masses of the coarse and feed materials are denoted by m_c and m_{feed}, respectively. The particle density distributions of the coarse and feed materials are denoted by q_c and q_{feed}, respectively.

$$T(x) = \frac{m_c}{m_{feed}} \cdot \frac{q_c(x)}{q_{feed}(x)} \cdot 100\% \quad (2)$$

As in [20], the experimental separation efficiency is corrected using Equation (3) [36,37]. This correction is intended to eliminate the division ratio, τ, present in the experimental separation curves, which results from the adhesion and incomplete dispersion of ultra-fine particles rather than the classifier's performance. Consequently, agglomerated fine particles behave as coarse material and may exist in the coarse material fraction after the separation process. Therefore, T(x) does not drop to zero for the finest particles, resulting in a division ratio, τ, (distance from zero line). This correction also facilitates a comparison with the CFD results, where the particles are fully dispersed, and no division ratio exists. In Equation (3), $T^*(x)$ and $T(x)$ represent the separation efficiency before and after correction, respectively.

$$T(x) = \frac{T^*(x) - \tau}{1 - \tau} \quad (3)$$

The separation sharpness, denoted as k (Equation (4)), is typically characterized as the ratio between particle sizes at two distinct separation efficiencies as follows: 25% (x_{25}) and 75% (x_{75}), obtained from the corrected separation curves.

$$k = \frac{x_{25}}{x_{75}} \quad (4)$$

2. Considerations of the Experimental Setup and Simulation

2.1. Experimental System Setup

This study utilized a homemade horizontal deflector wheel classifier with a vertical axis of rotation. The classifier has 16 airflow inlet nozzles distributed around the perimeter, arranged tangentially to the circumference at the tip of the blades. Four of the sixteen inlets are used to feed airborne particles (aerosol inlets), while the remaining twelve are for particle dispersion. The rotating wheel has 24 blades with a height of 40 mm. However, in contrast to other classifier designs, no stationary blades were used here.

In this investigation, two different blade designs of the deflector wheel were used (Figure 2), each with a different length, resulting in distinct sizes of the inner annular region due to their varying inner radii. The classifier casing has a radius of 125 mm. Both blade designs share an outer radius of 100 mm but possess different inner radii of 60 mm (case labeled as 60–100) and 35 mm (case labeled as 35–100), respectively.

In the second part of the study, the extended blades are integrated into experiments with an electrostatic separator to enable a two-dimensional separation process. Particles from two distinct materials are introduced into the classifier system. These particles

undergo triboelectric charging upon colliding with the walls of the classification system, as well as the dispersion system (RODOS).

This dispersion system operates on an injector concept, resulting in intense collisions between particles and the disperser wall. The same disperser system was previously employed in [13] as a particle triboelectric charger, where the mechanism of particle charging was explored through adjustments in parameters such as mass loading and flow rates. In the current study, different parameters are also varied to explore the interplay between particle classification, triboelectric charging, and material sorting. For all experiments, a mass loading below 1%, i.e., powder mass per air mass, is maintained.

The entire classification system, coupled with the material sorting apparatus, is depicted in Figure 1. The experimental setup comprises a feeder that delivers material to a disperser, where the particles are dispersed and precharged through collisions with the disperser walls. The particles then enter the classifier. Deflector wheel classifiers primarily consist of rotating blades that produce a circumferential motion of the flow in the surroundings. This circumferential motion results in centrifugal forces on the particles that direct them to the outer space. Additionally, the air entering the classifier and sucked from the center of the classifier produces drag forces on the particles that direct them to the center of the classifier. Theoretically, centrifugal forces acting on the coarse particles (typically bigger than the separation cut size) are greater than the drag forces, while the drag forces acting on the fine particles (typically smaller than the separation cut size) are greater than the centrifugal forces. Therefore, coarse particles exit the classifier at the bottom of the outer space due to the relatively high centrifugal forces acting on them. Conversely, fine materials are drawn towards the center of the classifier by the relatively high drag forces acting on them. Further details about the classifier design can be found in [14,20], where the same classifier has been investigated.

During classification, particles are triboelectrically charged through collisions with classifier walls. The charged fine materials are then directed into an electrostatic precipitator (ESP), where the two differently triboelectrically charged materials are separated and collected on both separator electrodes. From the fraction of deposited powder on each electrode and the operating conditions of the ESP, the mass-specific particle charge can be deduced by applying the Deutsch equation [14], which is as follows:

$$E_{+/-(x)} = \alpha_{+/-}(1 - \exp(-D)) \tag{5}$$

where $E_{+/-}$ is a dimensionless quantity and describes the degree of deposition of each particle of size x on an electrode. This indicates which fraction of a specific particle size class is deposited on each electrode, and D is the Deutsch number, defined as follows [38]:

$$D = \frac{wL}{sv} = \frac{\Delta U \bar{q} L}{3\pi\eta x \dot{V}} \tag{6}$$

where L is the electrode length, ΔU is the applied voltage, w is the particle migration velocity towards the electrodes, s is the side length of the quadratic channel, v is the average axial gas velocity, η is the dynamic gas viscosity, x is the particle diameter, $\dot{V}$ is the volumetric gas flow rate, and $\bar{q}$ is the particle charge.

From the measured density size distribution, q_3, of the powders deposited on the anode and cathode, the separation curves can also be calculated by Equation (7) using the feed density size distribution $q_{3,feed(x)}$, as follows [14]:

$$E_{+/-(x)} = \alpha_{+/-} \frac{q_{3+/-(x)}}{q_{3,feed(x)}} \tag{7}$$

where $\alpha_{+/-}$ is the asymptotic mass fraction (obtained for either infinitely long electrodes or infinitely high voltage). The values of $\alpha_{+/-}$ can be obtained by fitting Equation (5) to the data measured at different applied voltages ΔU [14] (refer to Section 3.2).

Unseparated particles exit the ESP and are collected in a cyclone separator. In cases where material sorting is not performed, the electrostatic separator is omitted from the configuration, and the fine materials are collected in the cyclone separator directly after the classifier.

The materials used in this study are Saxolith 2 (limestone), primarily composed of calcium carbonate, and talcum, which is composed of magnesium silicate. For the particle classifications in the first part of the study, Saxolith 2 is used. In the experiments for material sorting, a mixture comprising 50% by mass of each of Saxolith 2 and talcum powders is used. These two materials were selected due to their similar size and density characteristics. Saxolith 2 and talcum exhibit densities of 2.7 g/cm^3 and 2.75 g/cm^3, respectively. This choice aims to minimize the influence of particle size on electrostatic separation, ensuring that any observed separation effects are primarily due to differences in triboelectric charging rather than variations in particle size.

The cumulative particle size distributions of both materials were measured with laser diffraction using a HELOS device (Sympatec Inc., Clausthal-Zellerfeld - Germany). The size distributions of the raw materials, shown in Figure 3, confirm that most of the particles are smaller than 10 µm.

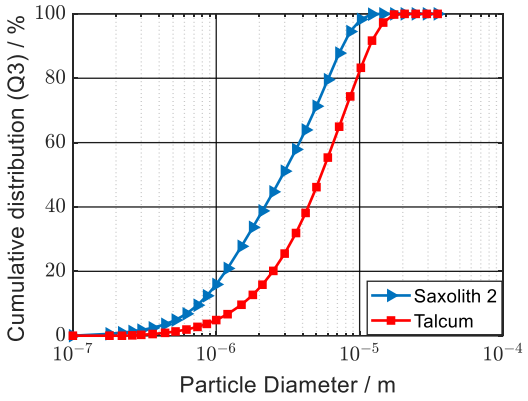

Figure 3. Particle size distribution of the powders used in the study.

2.2. Simulation Settings

As in [20], the computational fluid dynamics (CFD) analyses performed in this research utilized the ANSYS CFX 19.2 software, a commercial CFD solver specifically engineered for solving the Reynolds-Averaged Navier–Stokes (RANS) Equations. The simulations employed the Menter shear-stress transport (SST) turbulence model [39], which incorporates both the ($k-\varepsilon$ and $k-\omega$) two-equation turbulence models. This choice was made due to its effectiveness in predicting flow characteristics, particularly in boundary regions and throughout the bulk flow [11].

For the analysis of the dispersed phase, the discrete phase model (DPM) is employed, providing a comprehensive understanding of particle dynamics through both Lagrangian and discrete viewpoints [40]. The interaction between rotating blades and stationary components was managed using the multiple reference frame model (MRF), also known as the frozen rotor Generalized Grid Interface (GGI) approach, which is robust and offers computational efficiency compared to alternative approaches like the mixing plane approach [11]. Experimentally determined mass flow rates are used to define the boundary conditions for the aerosol inlet, and the fine and coarse material outlets. To ensure simulation robustness, the static pressure at the inlet of the dispersion flow is set to 1 bar, balancing the total inlet and outlet mass flow rates.

The flow rates in the simulations match those used in the experiments. Simulations use a discrete diameter distribution for particles at the classifier's inlet based on HELOS data.

This study employed a hybrid mesh, with tetrahedral elements in more complex regions and hexahedral elements in areas with simpler geometries. This method ensured

adequate accuracy in crucial areas while maximizing computational efficiency. Three different meshes were produced with a refinement ratio of about 2 to study grid independence. The refinement ratio is defined as the ratio between the grid spacing of the coarse and medium meshes, as well as between the medium and fine meshes. The total number of mesh elements is 10,243,185 for the coarse mesh, 19,387,890 for the medium mesh, and 37,655,375 for the fine mesh. Figure 4 provides an example of the grid independence achieved in the study. Figure 4a shows the distribution of the circumferential velocity of the air ($V\phi_a$) relative to the rotational speed of the blades ($V\phi_r$) from the blades' inlet to outlet, for the blades with the (60–100) configuration. The quantity ($V\phi_a - V\phi_r$) is a crucial parameter that defines the performance of the classifier and the flow uniformity in the blades region as discussed in [20]. The distributions of ($V\phi_a - V\phi_r$) within the blade channels, as shown in Figure 4a, were calculated using the three prespecified different meshes under the same operating conditions. Another crucial parameter for the classifier's performance is the pressure drop. Figure 4b shows the distribution of the total pressure across the classifier relative to that at the inlet of the classifier (P/P_{inlet}). Figure 4a,b show minor deviations between the calculations performed with the three different meshes, with all meshes producing the same flow pattern. These minor deviations observed in the distributions of $V\phi_a - V\phi_r$ and P/P_{inlet}, calculated across different mesh refinements, confirm grid independence. The finest mesh was used for further investigations in this study.

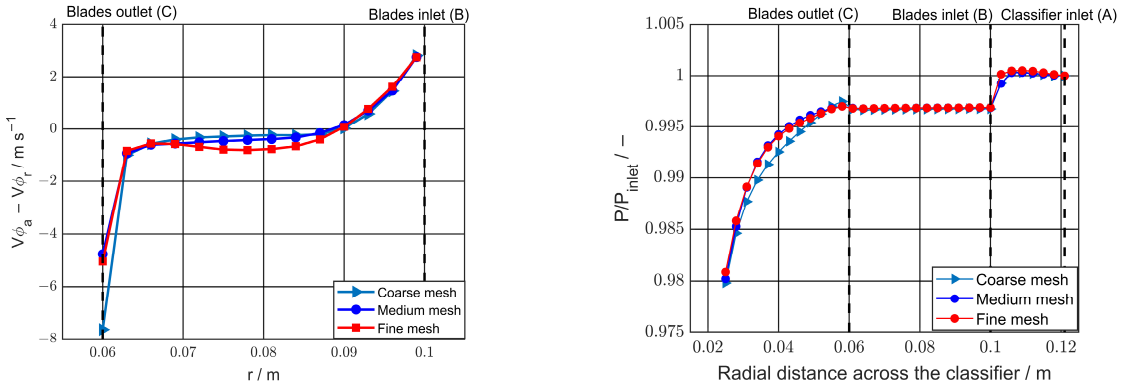

(**a**) Distribution of ($V\phi_a - V\phi_r$) within the blades channel (**b**) Distribution of P/P_{inlet} across the classifier

Figure 4. Three solutions obtained from three different mesh refinements with the same operating conditions, 5000 rpm and 72 m^3/h for the short blades (60–100); (**a**) difference in the circumferential velocities of air and rotor blades ($V\phi_a - V\phi_r$), (**b**) total pressure relative to total inlet pressure P/P_{inlet}.

3. Results and Discussion

In this section, we first explore the impact of blade length and the size of the annular inner region on the classification process, focusing particularly on enhancing the separation sharpness (k) (Equation (4)) and reducing the pressure losses. To achieve this, CFD simulations with integrated particle tracking are employed for thorough analysis. The obtained CFD results are then meticulously compared with corresponding experimental findings aimed at validating the accuracy of the CFD method.

Subsequently, we explore the interplay between particle classification and material sorting, and meticulously analyze the experimental results in this context.

3.1. Effects of Blade Length on Particles Classification Process and Pressure Drops

In Figure 5, the separation curves for two blade designs, namely (35–100) and (60–100), are presented at two different rotational speeds but with identical flow rates. Both the CFD separation curves (Figure 5a,b) and the corrected separation curves obtained from experimental data (corrected for the division ratio according to Equation (3), Figure 5c,d) exhibit consistent trends, showcasing the impact of blade length on separation sharpness.

Specifically, the longer blades (35–100) demonstrate higher separation sharpness compared to the shorter blades (60–100) across both operating parameters.

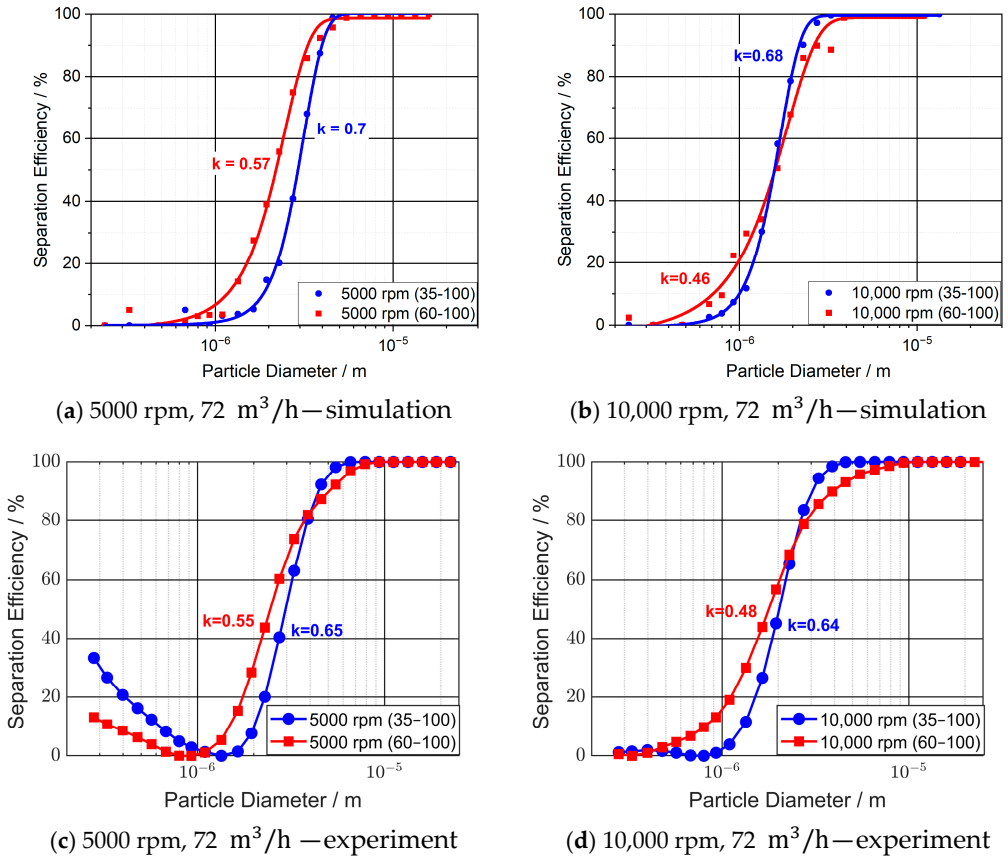

(**a**) 5000 rpm, 72 m^3/h—simulation (**b**) 10,000 rpm, 72 m^3/h—simulation

(**c**) 5000 rpm, 72 m^3/h —experiment (**d**) 10,000 rpm, 72 m^3/h—experiment

Figure 5. Separation curves obtained from CFD simulations (**a**,**b**) at a constant flow rate of 72 m^3/h and different rotational speeds of 5000 rpm (**a**) and 10,000 rpm (**b**), corrected separation curves obtained from experiments (**c**,**d**) at a constant flow rate of 72 m^3/h and different rotational speeds of 5000 rpm (**c**) and 10,000 rpm (**d**) (lines between points are Gaussian cumulative distribution fit only serving to guide the eye).

It is noteworthy that the separation sharpness of the shorter blades (60–100) dramatically reduces at higher rotational speeds and also at low flow rates, a phenomenon observed consistently in [20]. Conversely, the longer (35–100) blades maintain relatively high separation sharpness even at elevated rotational speeds. This indicates the robustness of longer blades in preserving separation efficiency, which is characterized by high separation sharpness (k) under varying operational conditions.

It is noteworthy that at 10,000 rpm, the fishhook effect, i.e., the increase in the separation efficiency with decreasing particle size [41–43], is almost eliminated compared to 5000 rpm for both case designs. This reduction in the fishhook effect can be attributed to the shift in the cut size toward finer particles at the higher rotational speed of 10,000 rpm. However, particle agglomeration at 10,000 rpm is indicated by the higher division ratio, τ, which is corrected using Equation (3).

Examining the flow characteristics for both cases is essential to understand the effect of the blade's length on the separation sharpness. Figure 6 illustrates velocity streamlines for both blade designs. In the (35–100) blades, flow vortices between the blades only occupy the outer part of the blade channel and extend to some point along the flow path, while for the (60–100) blades, these vortices persist throughout the blades' channels and occupy the whole length of the inter-blade channels. Additionally, the (60–100) blades exhibit larger regions of dead zone flow compared to the (35–100) blades.

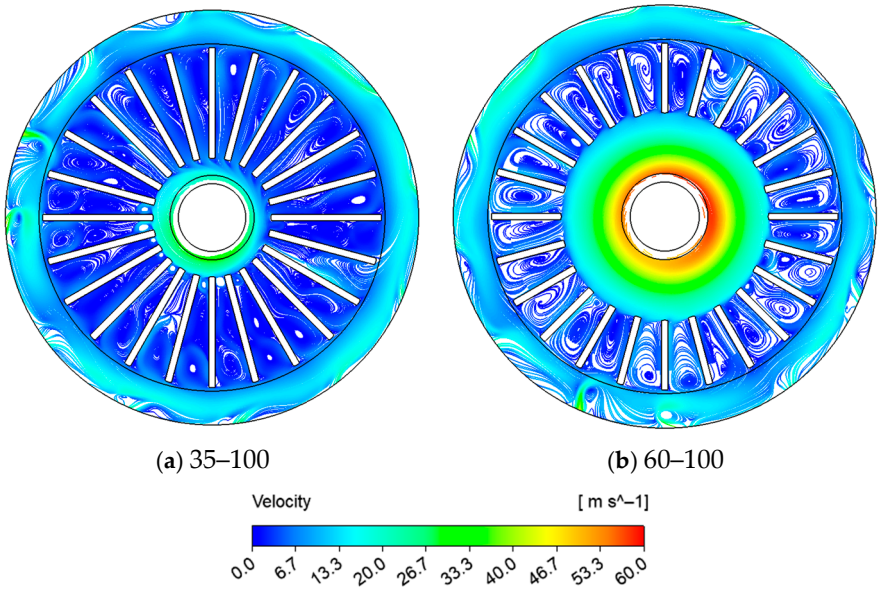

(**a**) 35–100 (**b**) 60–100

Figure 6. Velocity streamlines of air in the blades' channels for the two blade designs at 5000 rpm and 72 m^3/h.

Non-uniform flow distribution between the blades, as observed in the (60–100) case, can contribute to the deterioration of the classification process. Previous studies [20,30,31,33] have shown that this non-uniformity can cause the back-mixing of fine and coarse particles. However, it is not the only factor responsible for the low separation sharpness observed with the (60–100) blades.

The inner space of the classifier plays a significant role in this reduction in separation sharpness, as depicted in Figure 6. For the (60–100) blades, a higher circumferential velocity is generated within this region compared to the (35–100) blades. As noted in [10,11], the circumferential velocity in this region increases as the flow progresses toward the center of the classifier.

An additional classification zone may exist in this region, particularly prominent at higher rotational speeds. The emergence of this additional classification zone could diminish separation sharpness by increasing the randomness of particle movement within the classifier.

This effect is further illustrated in Figure 6a,b. As noted in [20], concepts elucidated in [23,44,45] suggest that a more uniform flow and, consequently, higher separation sharpness can be achieved when the disparity between the circumferential velocity of the flow and the rotor blades approaches zero.

The term $(V\phi_a - V\phi_r)$ represents this difference and is depicted for both blade designs from the blades' inlet (outer radius) to the blades' outlet (inner radius) at two different rotational speeds, as shown in Figure 7a. In Figure 7b, the absolute circumferential velocity $(V\phi_a)$ (circumferential velocity relative to a stationary frame of reference) for the same cases is represented from the classifier inlet to the center. It can be observed from the two figures that both blade designs exhibit almost the same profile of $(V\phi_a - V\phi_r)$ and $(V\phi_a)$, for as long as the flow exists within the blades channels; however, as the flow exits the blade channels, there is a significant disparity in circumferential velocity.

In Figure 7b, it is evident that the circumferential velocity of the flow within the blade channels experiences deceleration. As the flow exits the channels and enters the inner annular region, an increase in circumferential velocity occurs. In the case of (60–100), the flow exits the channels before undergoing sufficient deceleration, resulting in a relatively high circumferential velocity as it enters the annular region. Subsequently, it is further accelerated within that region.

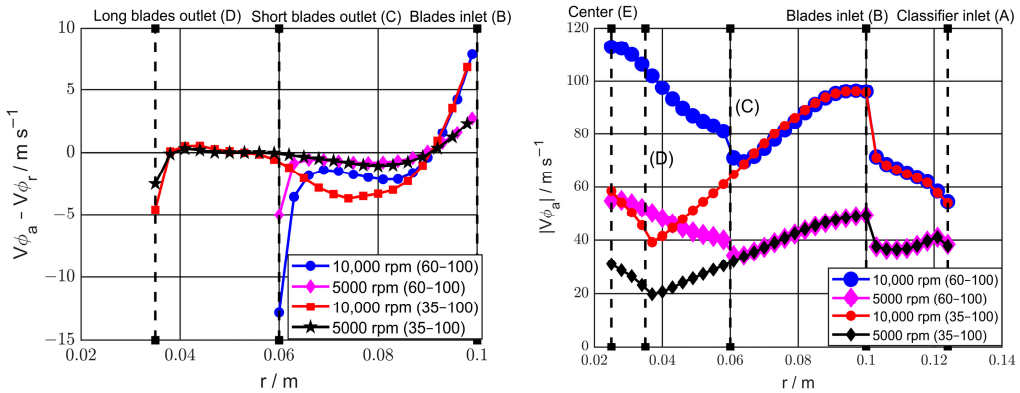

Figure 7. Circumferential velocity of the air represented relative to the rotating blades (**a**) and relative to a stationary frame of reference (absolute) (**b**) at different rotational speeds and with the same flow rate of 72 m^3/h. (**a**) Relative circumferential velocity between air and rotating blades in the blade's region. (**b**) Absolute circumferential velocity of the air from the classifier inlet (outer space, right side of the plot) to the center (left side of the plot).

Due to the very high circumferential velocity in that region, an additional classification zone is created, which becomes dominant at higher rotational speeds. This phenomenon may elucidate the observed shift in the cut size to be closer to the theoretical cut size calculated at the inner radius at higher rotational speeds in [20]. Extending the blades toward the center, as in the case of (35–100), would therefore provide more deceleration for the flow and reduce the size of the inner annular region. This, in turn, would prevent the flow from becoming highly accelerated again, thereby inhibiting the formation of a classification zone in this area and thus maintaining high separation sharpness.

This phenomenon is evident in the particle trajectories depicted in Figure 8, where trajectories from both case designs are shown for a sample of particles around the (x_{50}) that ultimately leave the classifier as coarse material. While these trajectories represent particles ultimately rejected to the outer space of the classifier, in the case of (60–100), the particles traverse through the outer annular region and the blade channels before reaching the inner annular region. Here, due to the high rotational speeds, the particles experience significant centrifugal forces, causing them to be rejected back into the outer space of the classifier. This phenomenon is not present for the (35–100) blades, indicating that no dominant classification zone is formed in the inner annular region in this case.

Table 1 presents the total pressure drops across the classifier in [Pa]. The pressure drop across the classifier is computed by subtracting the total pressure at the outlet from the total pressure at the inlet of the classifier. The (35–100) blades exhibit a reduction in pressure drop of up to 50% compared to the (60–100) blades. This reduction is attributed to the deceleration of the flow in the inner annular region, as illustrated in Figures 6 and 7. Elevated rotational speeds in this region lead to increased wall and viscous (internal) friction losses, resulting in higher pressure losses. Figure 4b shows that most of the pressure drop occurs in this region (from 0.06 m to the center). This increase in pressure drop is mitigated by extending the blades towards the interior of the classifier.

Table 1. Total pressure drops inside the classifier were determined from CFD simulations for different RPM designs.

Blades	5000 rpm	10,000 rpm
60–100	7045 [Pa]	23,207 [Pa]
35–100	3908 [Pa]	11,187 [Pa]

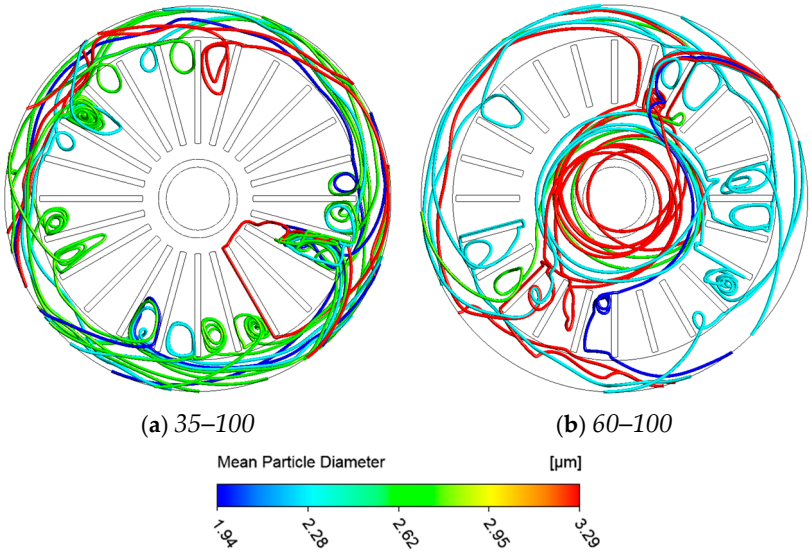

(**a**) *35–100* (**b**) *60–100*

Figure 8. Trajectories of particles ultimately leaving the classifier as coarse material at operational parameters of 5000 rpm and 72 m^3/h.

3.2. Triboelectric Particle Charging and Powder Separation in the ESP

The principle behind material sorting is rooted in the fact that different powders typically possess varying chemical compositions and, consequently, different work functions. This discrepancy in work function between particles and metal surfaces, or between different particles upon contact, facilitates charge transfer [7,13,46]. When various powders interact with a metal surface, they may either gain or lose electrons, resulting in a negative or positive charge. Moreover, the magnitude of charge acquisition post-contact can vary depending on the properties and work functions of the materials involved [47]. Leveraging this concept enables effective particle separation.

The powders investigated in this study are Saxolith 2 (calcite) and talcum (magnesium silicate), which exhibited distinct triboelectric charging behaviors upon contact with a steel wall (RODOS-disperser) in [13], where talcum demonstrated a negative charge while calcite exhibited a positive charge. In the current study, the two materials are introduced into the classification system as a 50% mixture, which includes the RODOS-disperser—the same one used in [13]—and the wheel classifier, where they are charged through collisions with the walls of these components.

Subsequently, material sorting can occur by introducing the charged materials into the electrostatic separator, where one electrode is positively charged and the other is grounded (cf. Figure 1, Part. 3). Based on the findings reported in reference [5], it is expected that the talcum particles tend to gather mostly at the positive electrode, while the Saxolith 2 particles predominantly collect at the grounded electrode.

The RODOS dispersing pressure, as well as the rotational speed and airflow rate of the classifier, are adjusted to examine particles' separation and charging behavior. The parameter combinations that were investigated are represented graphically in Appendix A.

Modifying the operating parameters of the classifier may result in a change in the cut size, which is determined by the radial and tangential airflow velocity at the blades. This, in turn, affects the size distribution of the particles introduced into the ESP. Figure 9a–c illustrates the impact of the modified parameter on the cut size.

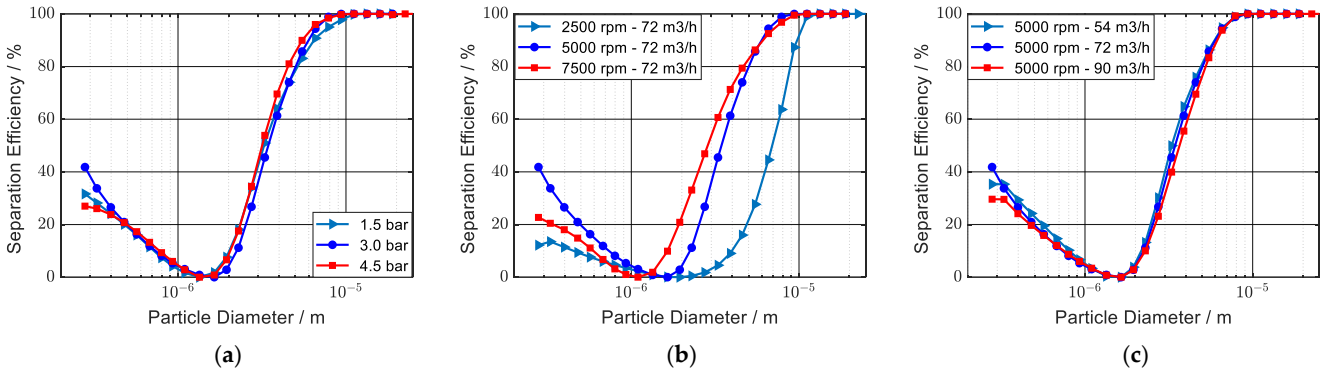

Figure 9. Separation curves (corrected) of the deflection wheel separator by varying (**a**) RODOS pressure at 5000 rpm, 72 m^3h^{-1}, (**b**) the rotational speed at 3 bar, 72 m^3h^{-1}, and (**c**) the air volume flow at 3 bar, 5000 rpm.

As the rotational speed remains constant, any changes in the flow rate or dispersion pressure have a minimal effect on the cut size of the separation (Figure 9a,c). However, as the rotational speed increases, the cut size noticeably shifts towards smaller particle sizes (Figure 9b).

Laser diffraction analysis is used to determine the particle size distribution of the collected material at the electrodes of the ESP. However, this distribution is based on an unknown mixture of both components. The proportions of Saxolith 2 and Talcum in the collected samples were determined using a chemical method based on the different reactions of the materials with hydrochloric acid [14]; Saxolith 2 ($CaCO_3$) reacts with acid while talcum does not. Known binary mixtures were dissolved in 0.50 M hydrochloric acid. After filtering and drying, the residue on the weighed filters was used to determine the Saxolith 2 and talcum contents to build a calibration curve (cf. Appendix B). The material contents in experimental samples are then calculated. To ascertain the size distributions of the individual components from the overall distribution, separation curves of the mixture at the electrodes (E+, E_{GND}) were computed and then merged with the mass fractions obtained from the dissolution tests.

Changing the voltage at the ESP allowed the calculation of the highest achievable positive and negative mass fractions of the individual materials, as shown in Figure 10, for Saxolith 2 and talcum. This demonstrates that talcum is more negatively charged (60.8%), whereas Saxolith 2 contains 59.7% positively charged particles. The percentages of the respective counter electrodes are also similar for both materials at approx. 19% for talcum and 17% for Saxolith 2.

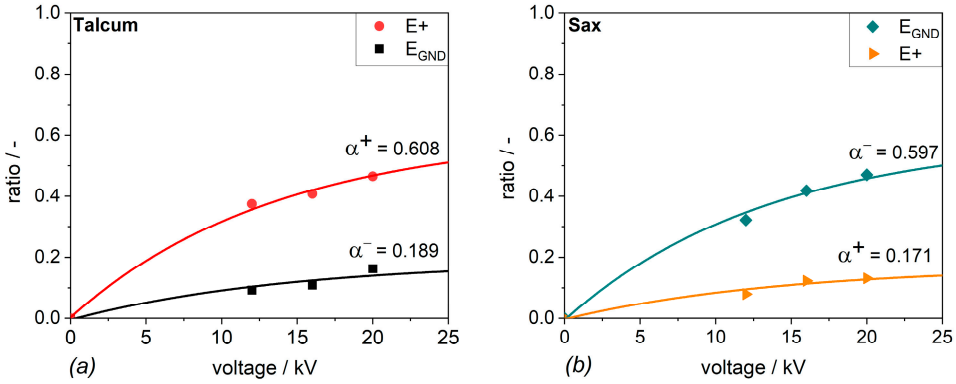

Figure 10. Enrichments of talcum (**a**) and Saxolith 2 (**b**) on E+ and E_{GND} as a function of the applied voltage on the ESP; operational parameter of the classifier: 5000 rpm and 72 m^3/h.

3.2.1. Effect of the Operational Parameters on the Particle Charge for Saxolith 2 and Talcum

Calculating the particle charge can be achieved by combining Equations (5)–(7) and the obtained mass fractions $\alpha_{+/-}$ at the electrodes for Saxolith 2 and talcum (cf. Figure 10a,b). However, it is essential to note that only the average particle charge may be inferred, given the quantities and size distribution of the deposited materials are measured across the whole length of the 0.75 m electrodes (cf. Figure 1 No. 3).

Figure 11 compares the mean particle charge for talcum when the RODOS disperser is used alone or in conjunction with the deflector wheel classifier.

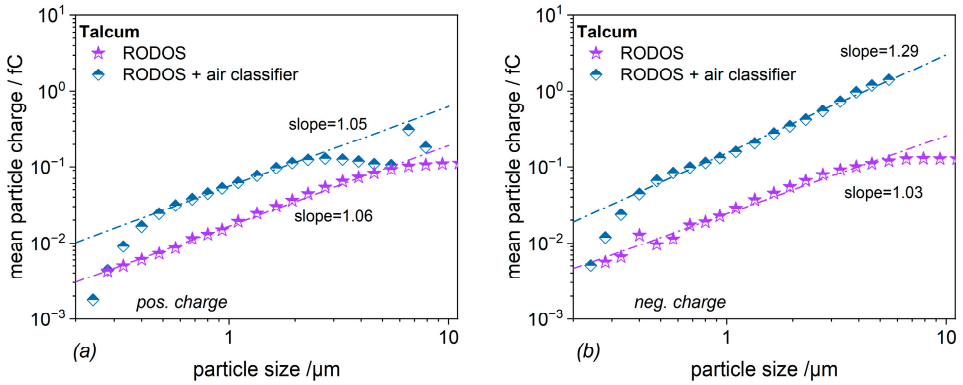

Figure 11. Mean particle charge for talcum using the RODOS disperser without the classifier periphery (half-filled asterisks) and in conjunction with the classifier (half-filled diamonds) for positively (**a**) and negatively charged (**b**) particles and the same mass particle loading. The dashed-dotted lines are linear fit-functions; RODOS pressure: 3 bar; classifier flow rate: 72 m^3h^{-1}; rotational speed: 5000 rpm.

When the RODOS is combined with the classifier, it greatly enhances the average charge of, e.g., 1 µm talcum particles—approximately 3.3 times more for positively charged particles and 5.5 times more for negatively charged particles. Smaller particles show identical charge behavior to larger ones if solely using the RODOS disperser. Still, when used in conjunction with the classifier, different charging characteristics for smaller and larger particles are exhibited, leading to a significantly reduced charge for particles up to 0.5 µm. In the RODOS, the material is mostly conveyed into the system as particle agglomerates, where it is mixed with air and accelerated utilizing a free jet. The particles' impact on the walls of the rectangular dispersing section disintegrates existing agglomerates. As agglomerates, even small particles may overcome the viscous boundary layer and collect charge due to intensive particle–wall contact. This leads to the consistent particle charging in the RODOS, showing a particle charge proportional to the particle size from the smallest (0.3 µm) to the largest (6 µm) observed size. Only for even larger particles (above 6 µm) does the particle charge become size-independent. However, in this size range, the number of particles is already greatly reduced, and the apparent results suffer from poor statistics.

The dispersed particles are fed into the wheel classifier by the particle inlet nozzle, which is made of brass, and exhibit an internal diameter of 6 mm and a length of 13.5 cm (cf. Figure A3, insert). The effect of the brass nozzle on the charging of talcum particles was investigated using an external experimental setup in the laboratory. In order to avoid the precharging of the particles during dispersion, talcum particles were dispersed by a small gas stream, then mixed with a larger gas stream and transported through the nozzle. The result in Appendix C shows that the small particles are slightly positively charged while the large particles are negatively charged, which correlates well with the findings in [13]. However, the charge per particle is at a low level, so the passage through the inlet nozzle can be regarded as negligible. In addition, the particle concentration in the brass nozzle during the laboratory investigation was lower by a factor of about 300 compared to the particle concentration in the inlet nozzle of the classifier. According to the literature [13,17,48], the

particle charge may be affected by particle mass loading, and this relationship follows a scaling law of approximately one divided by mass loading, i.e., at high mass loadings, the mass-specific charge of the powder is strongly reduced. The mass-specific charge is defined as the electric charge that particles carry per unit mass. Therefore, the particle charge acquired in the inlet nozzle of the classifier is substantially lower than the values shown in Figure A3. In summary, particle charging within the RODOS and in the inlet nozzle is relatively minor compared to the charging that occurs in the classifier itself.

The effects of the different operational parameters on the particle charge are discussed in the next step.

Figure 12 displays the mean particle charge when the pressure of the RODOS disperser is altered between 1.5 bar and 4.5 bar.

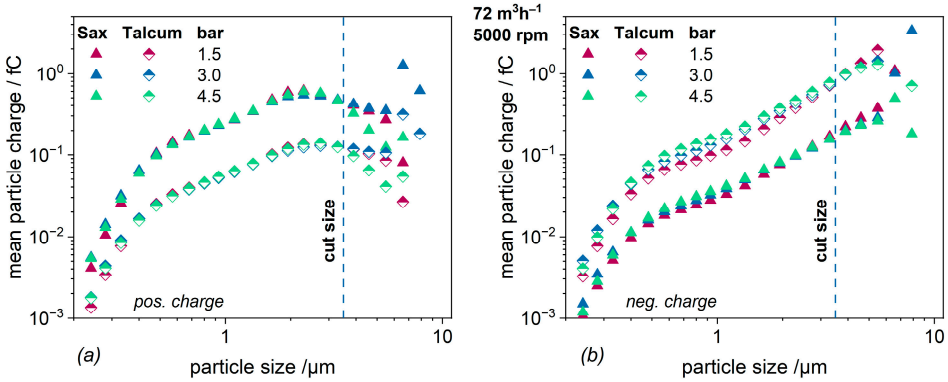

Figure 12. Mean particle charge of positively charged (**a**) and negatively charged (**b**) Saxolith 2 (filled triangles) and talcum (half-filled diamonds) particles for each size class at different RODOS pressures for a constant rotational speed of 5000 rpm and a constant flow rate of 72 m^3h^{-1}.

The impact of the RODOS pressure alone is minor since the charging process, as depicted in Figure 11, is mainly influenced by the classifier. During these experiments, the classifier was run at a constant rotational speed and flow rate, ensuring no particle charge alteration was expected.

Figure 13 illustrates the calculated mean particle charges for each size class of Saxolith 2 and talcum as the volume flow rates increase at a constant rotational speed of 5000 rpm (Figure 13a,b) and when the rotational speed increases at a constant flow rate of 72 m^3 h^{-1} (Figure 13c,d).

A 1.67-fold increase in the volume flow rate, from 54 to 90 m^3h^{-1}, results in approximately doubling the average particle charge within the size range of 0.5 µm to the cut size for both materials and polarities. Since charge transfer mainly occurs during particle–wall collisions, this behavior appears to be caused by the increased or more intensive collisions of the particles with the blades of the classifier wheel, resulting in a higher particle charge.

Although an increase in volume flow rate minimally affects the cut size, it is reduced from 7 µm to approximately 3 µm when the rotational speed is tripled from 2500 rpm to 7500 rpm (cf. Figure 9b,c). However, it is impossible to establish a clear relationship between the average particle charge and the rotational speed. Figure 7a demonstrates that as the rotational speed increases, the flow field between the blades becomes more non-uniform, which may result in a more complex turbulence level and unpredictable effects on the impacts of particles on the wall. This is further underlined by the illustration of the averaged eddy viscosity in Appendix D, which demonstrates that the intensity of turbulence in the classifier's gap, i.e., the ring between the deflection wheel and the enclosing device wall and between the blades, may significantly fluctuate depending on the operational condition. The turbulent viscosity is responsible for the turbulent diffusion transport and, therefore, influences the trajectory of the particles, especially near the boundary layer, and thus the impact of the particles on the wall. Increasing the rotational speed results in more intense particle–wall collisions, even for smaller particles, which, in turn, reduces the cut

size. The remaining particles in the classifier may be carried away from the wall by the energy of the vortex, reducing the frequency of collisions. Grosshans [49] describes the particle charging process during the turbulent, pneumatic transport of particles in pipes. It is shown that particles with low Stokes numbers (0.2) accumulate in the central region of the pipe flow (away from the boundary layer). In contrast, particles with higher Stokes numbers exhibit a displacement of the highest particle concentration towards the wall of the pipe.

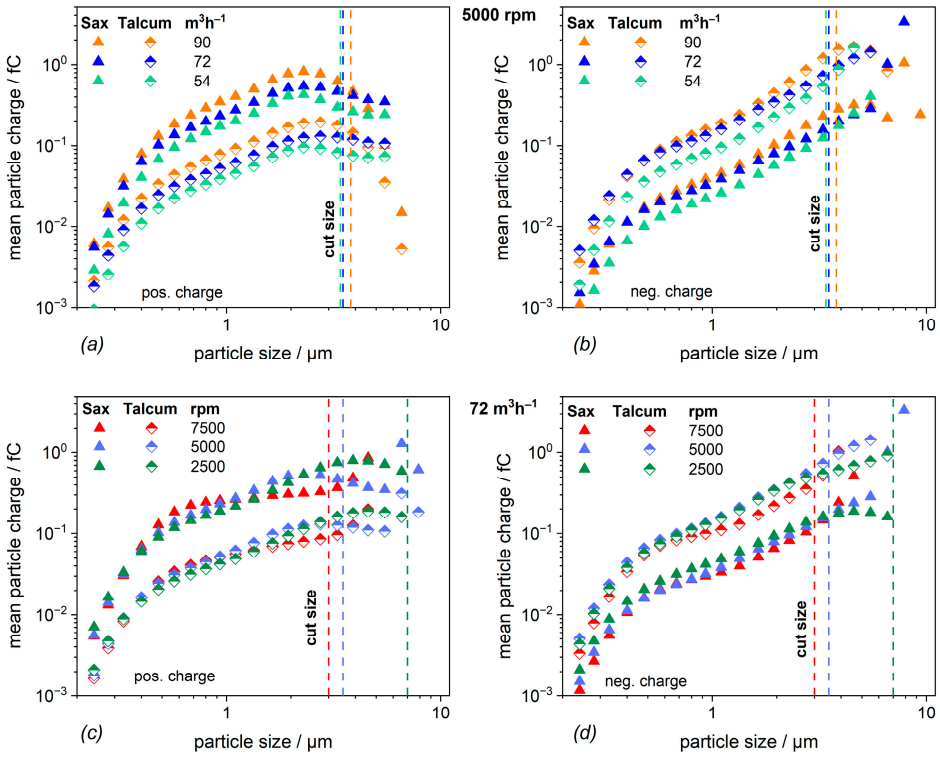

Figure 13. Mean particle charge of positively charged (**a**,**c**) and negatively charged (**b**,**d**) Saxolith 2 (filled triangles) and talcum (half-filled diamonds) particles for each size class. **Top line:** different flow rates at a constant rotational speed of 5000 rpm; **bottom line:** different rotational speed at a constant flow rate of 72 m^3h^{-1}; the dashed vertical lines represent the corresponding cut sizes for the different flow rates and rotational speed (cf. Figure 9).

On the other hand, the cut size shifts toward smaller particle sizes, resulting in a higher volume concentration of particles in the classifier gap as more particles are deflected. This may result in a higher likelihood of particle–particle contact upon their entry into the classifier, which may contribute to charge transfer or charge equalization.

The complex flow field parameters may affect the particle charging process in such a way as to explain the nearly linear behavior of the mean particle charge with respect to particle size. However, to capture the exact behavior of the particles, a detailed model for the particle movement in the boundary layer flow would be necessary, which is beyond the scope of this investigation. Therefore, the experimental finding that the particle charge increases slightly more than linearly with the particle diameter in the classifier system under consideration is noted.

3.2.2. Effect of the Operational Parameters on the Specific Charge of Saxolith 2 and Talcum

As mentioned in Section 2, the Deutsch number may be used to calculate the specific charge. The calculated mean particle charge is combined with the corresponding masses deposited on the positive and negative electrodes, whereby the mass in the cyclone is also considered. With this calculation procedure, the particle charge in response to the variations in the classifier operating parameters is determined as shown in Figure 14.

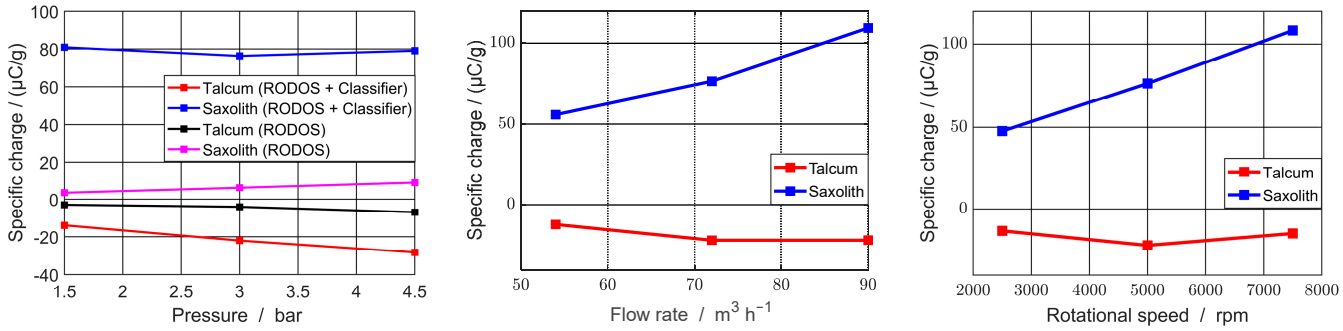

Figure 14. Corresponding specific powder charge for variations in dispersion pressure, flow rate, and rotational speed. (**a**) Dispersion pressure variations at constant 5000 rpm and 72 m^3h^{-1}. (**b**) Flow rate variations at constant 5000 rpm and 3 bar of RODOS pressure. (**c**) Rotational speed variations at constant 72 m^3h^{-1} and 3 bar of RODOS pressure.

Figure 14a demonstrates the impact of the deflector wheel classifier on the specific charge of both materials relative to the RODOS disperser alone [13,14]. In turn, the deflection wheel separator significantly increases the overall powder charge. For Saxolith 2, the specific charge rises 8- to 10-fold, whereas for talcum particles, it rises 6-fold after the separating process. Additionally, varying the dispersion pressure did not significantly increase the specific charge, and consequently, the dispersion pressure was kept constant at 3 bar for all experiments, shown in Figure 14b,c.

The specific particle charge for Saxolith 2 increases a lot with engine speed and flow rate (flow speed) (see Figure 14b,c). With increasing flow rate, the mean particle charge also increases, even though the cut size shifted slightly towards a larger particle size (cf. Figure 9). As the rotational speed increases, the mean particle charge slightly decreases. However, this specific charge operates in the opposite direction, as reducing cut size results in a lower mass of individual fine particles and, consequently, an increase in the charge-to-mass ratio.

Figure 14 shows that the measured charge of Saxolith 2 exceeds that of talcum. Since the particles of both materials exhibit a similar collision behavior in the classifier (similar density and shape), this discrepancy in measured charge can be attributed solely to the work functions of the two materials and the contact material (the classifier blades) when using the so-called condenser model for the particle–wall contact [50].

This phenomenon can be further explained by considering the work functions of the elemental materials involved in the triboelectrification process. According to [51], the work function of Al_2O_3, representing the contact material of the classifier blades, is 4.7 eV. The same value of 4.7 eV is also obtained for MgO, representing a main component of the talcum powder. In contrast, Saxolith 2 powder (mainly composed of calcite) can exhibit a lower work function, ranging between 4.26 and 4.55 eV [52,53]. Based on these work function values, Saxolith 2 is expected to acquire a positive charge in contact with Al_2O_3, while talcum would exhibit a minimal charge transfer. The charge obtained by talcum seems to be attributed to contact with the classifier's stainless-steel walls rather than the blades.

Therefore, the deflector wheel classifier in the present setup appears to be a suitable device for simultaneous classification and particle charging. Finally, it remains to be shown that the size-classified and triboelectrically charged particles can be sorted by material in the subsequent ESP. This is shown in the next section for separating talcum and Saxolith 2 powder.

3.3. Sorting of the Two Materials in the ESP

As outlined in Section 2, materials are collected at four distinct positions as follows: the coarse material outlet and three positions for the fine materials—specifically, the electrode where high voltage is applied (E^+, HV, deposition of negatively charged particles), the

grounded electrode (E_{GND}, deposition of positively charged particles), and the remaining material collected in the cyclone (mostly neutral particles). The enrichments of the two materials at these positions are depicted in Figure 15 for the operating condition with 7500 rpm, 72 m^3/h, and 3 bar. At other operating conditions, similar enrichments of the two materials are obtained with slight deviations of the maximum of approximately 5–10%.

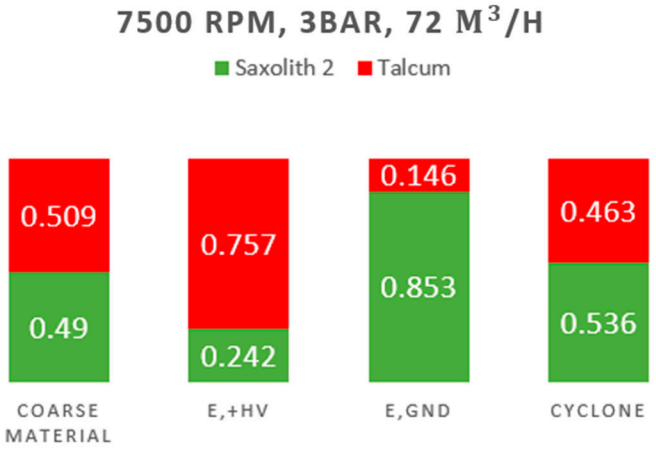

Figure 15. Enrichments of Saxolith 2 and talcum at different positions, including coarse material outlet, both electrodes, and the cyclone.

Figure 15 indicates that both materials contain almost 50% of the total mass in the coarse material. As expected, fine material is effectively separated onto both electrodes; talcum is collected on the electrode with an applied positive voltage, while Saxolith 2 accumulates on the grounded electrode, with both materials exhibiting an enrichment of approximately 25–35%. Unseparated materials from both groups are collected in the cyclone, each accounting for almost 50% of the total mass. The nearly identical material composition of the cyclone compared to the coarse material may be attributed to the fact that talcum and Saxolith 2 have nearly the same $\alpha_{+/-}$ value, albeit with opposite polarities (cf. Figure 10).

Adjusting the electrical field strength in the ESP may achieve further enrichment. Figure 16 illustrates the calculated electrical mobility from the mean particle charge for one operating condition and three iso-mobility lines (increasing field strength from 1 to 3). The electrical mobility is determined by the migration velocity of a charged particle (size x, charge $\bar{q}$) in an electric field E, according to Equation (8) [14].

$$Z = \frac{\bar{q}}{3\pi\eta x} \tag{8}$$

Particles exhibiting identical mobility within the same electric field will achieve the same migration velocity, resulting in an equivalent degree of deposition.

By adjusting the field strength in the ESP to align with iso-mobility line 1 or 2, efficient separation of positively charged Saxolith 2 particles from talcum particles may be achieved. A lower field strength above line 1 results in the deposition of Saxolith 2 with high purity at the negative electrode. However, losses occur in the outer areas of the distribution ($x < 0.5$ µm or $x > 2$ µm), as the particles are not mobile enough to be separated and instead enter the downstream cyclone. A higher field strength, demonstrated by line 3, minimizes the mass losses of Saxolith 2 and talcum, respectively. But this also leads to decreasing selectivity, as the less mobile talcum particles may now be deposited on the electrodes.

The migration velocity is determined by the product of electrical mobility, electrical field strength, and geometric channel dimensions, such as the length and width of the ESP. Adjusting the channel dimensions may be necessary to reduce the mass lost when a high level of enrichment is required.

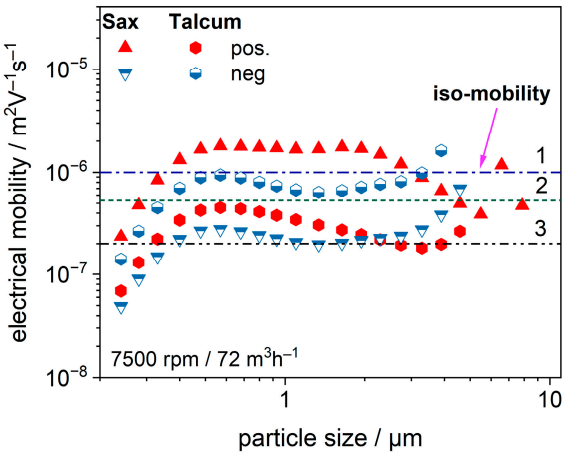

Figure 16. Electrical mobility for negative (half-filled symbols) and positive (filled symbols) charged Saxolith 2 (triangles) and talcum (diamonds) particles; lines 1 to 3: artificial iso-mobility lines corresponding to an increasing electrical field strength from 1 (lowest) to 3 (strongest).

The charge and the sorting of material obtained in this study are due to natural triboelectrification, where no voltage is applied to the contact material. By applying a high voltage on the contact material (forced triboelectrification), the charge and the separation behavior of the material may be changed, as represented in previous works [7,53]. Thus, the deflector wheel classifier seems to be a good tool for material sorting and simultaneous size-based particle classification.

Concerning the efficient material separation, it may be concluded that an increased flow rate in the classifier combined with a reduced electric field strength in the electrostatic precipitator can lead to a significant accumulation of Saxolith 2 on the E_{GND} electrode. This effect is attributed to the higher positive charge of the Saxolith 2 particles. A similar conclusion may also be formulated for the negative particles deposited on the E+ electrode.

4. Conclusions

In this study, we explore a method for two-dimensional particle separation based on size and material sorting using an integrated air classifier and electrostatic separator. The first part of the study focuses on optimizing the classifier for particle classification by adjusting blade length. In the second part, we present the results of the two-dimensional separation. Below are the main conclusions:

1. Longer blades, extending towards the classifier's center, enhance separation sharpness compared to shorter blades.
2. Blade extension reduces the inner annular region size, minimizing high-velocity vortex formation.
3. Vortex formation in this region creates an additional classification zone, reducing sharpness, especially at high rotational speeds and increasing pressure drop.
4. The classifier can significantly contribute to particle charging and can be successfully utilized for material sorting.
5. If the difference in the work function between the particles and the contact walls is significant, variations in the rotational speed and flow rate can lead to changes in the specific charge of the particles.
6. Increasing the volume flow rate increases the acquired mean particle charge and the specific charge in the classifier.
7. Increasing the blade's rotational speed increases the acquired specific charge.
8. Adjusting the electric field strength in the ESP can achieve material sorting of different powder materials.

Author Contributions: Conceptualization, M.A., A.W. and A.P.W.; methodology, M.A. and A.P.; software, M.A.; validation, M.A., A.W. and B.B.; formal analysis, M.A., A.W. and M.J.; investigation, M.A. and A.P.; resources, M.A. and B.B.; data curation, M.A. and M.J.; writing—original draft preparation, M.A. and A.W.; writing—review and editing, A.P.W., A.W., B.B., A.P. and M.J.; visualization, M.A.; supervision, A.P.W.; project administration, A.P.W.; funding acquisition, A.P.W. All authors have read and agreed to the published version of the manuscript.

Funding: This research was funded by the German Research Foundation (DFG) (grant number: WE 2331/22-2) within the Priority Program 2045.

Data Availability Statement: The data are available upon reasonable request from the corresponding author.

Acknowledgments: We express our gratitude to Leonard Hansen for manufacturing the classifier used in this study. We acknowledge financial support from Open Access Publishing Fund of Clausthal University of Technology.

Conflicts of Interest: The authors declare no conflicts of interest. The funders had no role in the design of the study; in the collection, analyses, or interpretation of the data; in the writing of the manuscript; or in the decision to publish the results.

Appendix A

The fractional factor design, shown in Figure A1, was used to investigate the impact of various operational parameters and the effect of the dispersion on the cut size, particle charging, and material sorting.

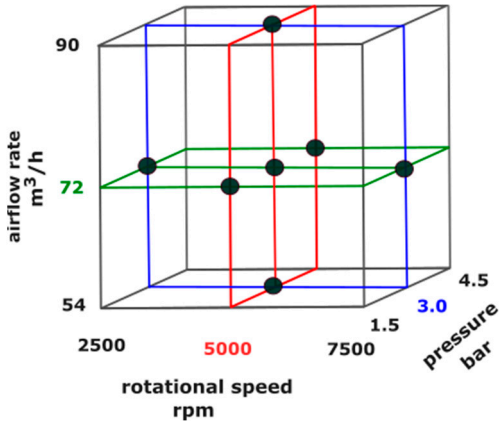

Figure A1. Parameter combination for the experiments (standard parameter: 5000 rpm, 72 m^3/h, 3 bar) (black spherical points in the figure represent the outperformed experiments).

Appendix B

The calibration curve used to determine the contents of Saxolith 2 and talcum after the sorting process is shown in Figure A2.

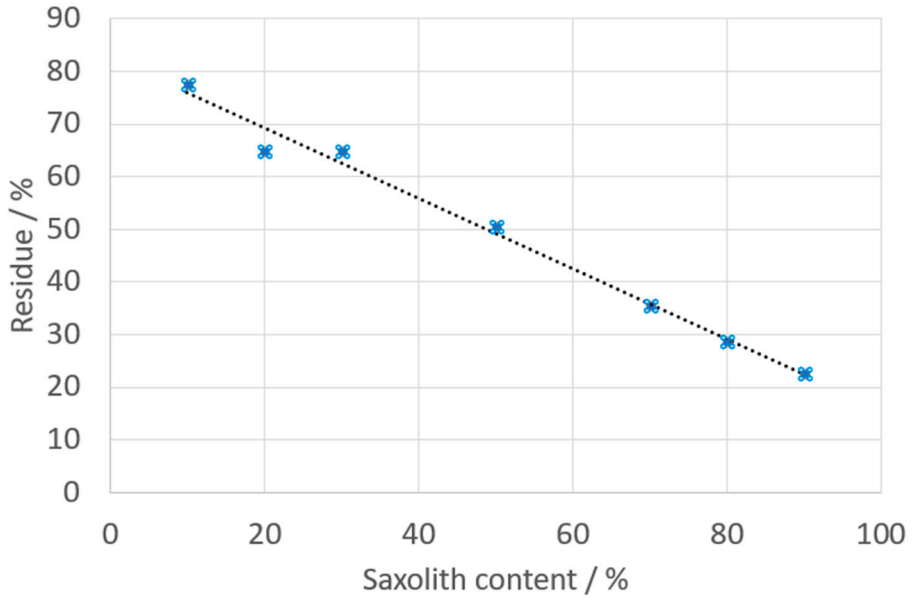

Figure A2. Calibration of the residue of material to the Saxolith 2 content.

Appendix C

The Electrical Low-Pressure Impactor ELPI+® (DEKATI) [54] measurement of talcum particles in Figure A3 reveals, by turning on and off the corona charger, the net charge per particle. According to the studies conducted by Ose [48], Hansen et al. [13], and Watano [17], it is observed that the charge magnitude increases as the particle mass loading decreases, and it follows a scaling relationship of approximately 1/mass loading. In this particular case, the particle mass loading per nozzle is 1/300 of the mass loading in the actual classifier inlet. Consequently, the measured net charge might be higher in this scenario compared to Figure 11.

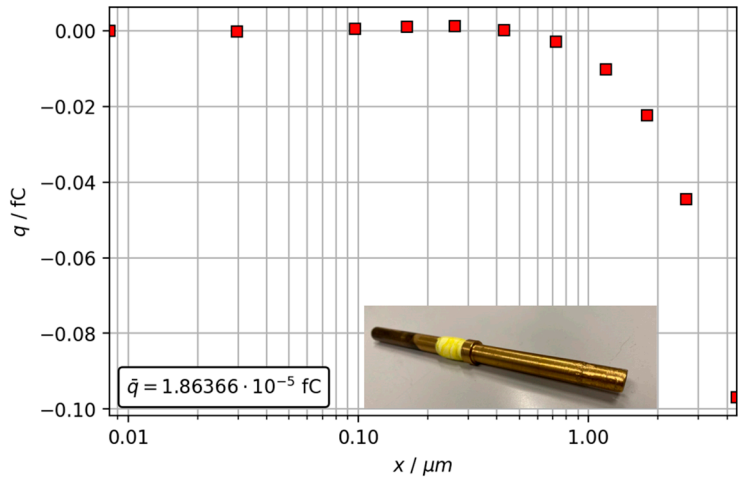

Figure A3. Net charge per particle for talcum in contact with brass nozzle (with a photograph of the nozzle as insert: length 13.5 cm and 6 mm inner diameter).

Appendix D

The distribution of the eddy viscosity within the flow through the classifier reveals that the classifier's operating parameters can significantly influence the intensity of turbulence. This, in turn, affects the trajectories of the particles, leading to variations in particle impact behavior on the walls. Eddy viscosity is an effective viscosity in turbulent flow that quantifies the increased momentum transfer caused by the chaotic motion of eddies. The

eddy viscosity μ_T is given by Equation (A1) [55], where $\overline{S_{ij}}$ is the Reynolds-averaged strain-rate tensor, k is the turbulent kinetic energy, and δ_{ij} is the Kronecker delta.

$$-\rho\overline{v_i'v_j'} = 2\mu_T\overline{S_{ij}} - \frac{2}{3}\rho k\delta_{ij} \quad \text{(A1)}$$

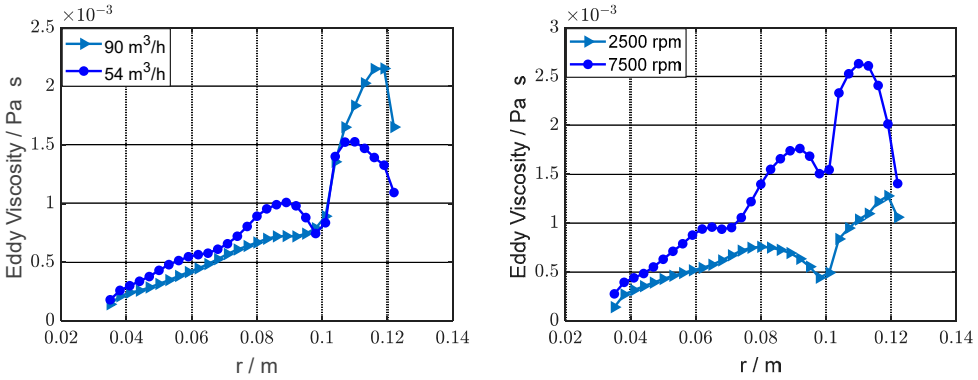

Figure A4. Turbulent (eddy) viscosity of the air from classifier inlet (outer space) to the center of the classifier at different flow rates (**a**) and at different rotational speeds (**b**) calculated using CFD simulations. (**a**) Turbulent viscosity of the air at different flow rates and constant 5000 rpm. (**b**) Turbulent viscosity of the air at different rotational speeds and constant 72 m^3h^{-1}.

References

1. Gu, Y.; Xia, K.; Wu, D.; Mou, J.; Zheng, S. Technical Characteristics and Wear-Resistant Mechanism of Nano Coatings: A Review. *Coatings* **2020**, *10*, 233. [CrossRef]
2. Parthasarathy, M. Challenges and Emerging Trends in Toner Waste Recycling: A Review. *Recycling* **2021**, *6*, 57. [CrossRef]
3. Masuhr, M.; Kruis, F.E. Fractionation of Aerosols by Particle Size and Material Composition Using a Classifying Aerodynamic Lens. *Powders* **2024**, *3*, 392–415. [CrossRef]
4. Giesler, J.; Weirauch, L.; Thöming, J.; Baune, M.; Pesch, G.R. Separating microparticles by material and size using dielectrophoretic chromatography with frequency modulation. *Sci. Rep.* **2021**, *11*, 16861. [CrossRef]
5. Sajeesh, P.; Sen, A.K. Particle separation and sorting in microfluidic devices: A review. *Microfluid. Nanofluid.* **2014**, *17*, 1–52. [CrossRef]
6. Xie, S.; Hu, Z.; Lu, D.; Zhao, Y. Dry Permanent Magnetic Separator: Present Status and Future Prospects. *Minerals* **2022**, *12*, 1251. [CrossRef]
7. Javadi, M.; Abohelwa, M.; Wollmann, A.; Weber, A.P. Dry Recycling of Lithium-Containing Material by Forced Tribocharging and Electrostatic Separation. *Chem. Ing. Tech.* **2024**, *96*, 950–957. [CrossRef]
8. Javadi, M.; Abohelwa, M.; Wollmann, A.; Weber, A.P. Characteristics of Powder Charging Behavior via Forced Triboelectric Charging on an Inclined Chute. *Powder Technol.* **2024**, *in press*. [CrossRef]
9. Zeng, Y.; Huang, B.; Qin, D.; Zhou, S.; Li, M. Numerical and Experiment Investigation on Novel Guide Vane Structures of Turbo Air Classifier. *Processes* **2022**, *10*, 844. [CrossRef]
10. Betz, M.; Gleiss, M.; Nirschl, H. Effects of Flow Baffles on Flow Profile, Pressure Drop and Classification Performance in Classifiers. *Processes* **2021**, *9*, 1213. [CrossRef]
11. Toneva, P.; Epple, P.; Breuer, M. Grinding in an air classifier mill—Part I: Characterisation of the one-phase flow. *Powder Technol.* **2011**, *211*, 19–27. [CrossRef]
12. Spötter, C. Dynamik der Trenncharakteristik eines Abweiseradsichters. Doctoral Thesis, Technische Universität Clausthal, Papierflieger Verlag, Germany, 2018.
13. Hansen, L.; Wollmann, A.; Weers, M.; Benker, B.; Weber, A.P. Triboelectric Charging and Separation of Fine Powder Mixtures. *Chem. Eng. Technol.* **2020**, *43*, 933–941. [CrossRef]
14. Hansen, L. *Analyse Eines Abweiseradsichters in Kombination Mit Einem Triboelektrischen Materialsortierer*; Technische Universität Clausthal: Clausthal-Zellerfeld, Germany, 2023.
15. Matsusaka, S.; Maruyama, H.; Matsuyama, T.; Ghadiri, M. Triboelectric charging of powders: A review. *Chem. Eng. Sci.* **2010**, *55*, 5781–5807. [CrossRef]
16. Li, J.; Yao, J.; Zhao, Y.; Wang, C.-H. Large eddy simulation of electrostatic effect on particle transport in particle-laden turbulent pipe flows. *J. Electrost.* **2021**, *109*, 103542. [CrossRef]
17. Watano, S.; Saito, S.; Suzuki, T. Numerical simulation of electrostatic charge in powder pneumatic conveying process. *Powder Technol.* **2003**, *135–136*, 112–117. [CrossRef]

18. Masui, N.; Murata, Y. Electrification of polymer particles by impact on a metal plate. *Jpn. J. Appl. Phys.* **1983**, *22*, 1057. [CrossRef]
19. Matsusaka, S.; Ghadiri, M.; Masuda, H. Electrification of an elastic sphere by repeated impacts on a metal plate. *J. Phys. D Appl. Phys.* **2000**, *33*, 2311. [CrossRef]
20. Abohelwa, M.; Benker, B.; Javadi, M.; Wollmann, A.; Weber, A.P. Limitation in the Performance of Fine Powder Separation in a Turbo Air Classifier. *Processes* **2023**, *11*, 2817. [CrossRef]
21. Toneva, P.; Wirth, K.-E.; Peukert, W. Grinding in an air classifier mill—Part II: Characterisation of the two-phase flow. *Powder Technol.* **2011**, *211*, 28–37. [CrossRef]
22. Denmud, N.; Baite, K.; Plookphol, T.; Janudom, S. Effects of Operating Parameters on the Cut Size of Turbo Air Classifier for Particle Size Classification of SAC305 Lead-Free Solder Powder. *Processes* **2019**, *7*, 427. [CrossRef]
23. Feng, Y.; Liu, J.; Liu, S. Effects of operating parameters on flow field in a turbo air classifier. *Miner. Eng.* **2008**, *21*, 598–604. [CrossRef]
24. Gao, L.; Yu, Y.; Liu, J. Study on the cut size of a turbo air classifier. *Powder Technol.* **2013**, *237*, 520–528. [CrossRef]
25. Zeng, Y.; Zhang, S.; Zhou, Y.; Li, M. Numerical Simulation of a Flow Field in a Turbo Air Classifier and Optimization of the Process Parameters. *Processes* **2020**, *8*, 237. [CrossRef]
26. Huang, Q.; Liu, J.; Yu, Y. Turbo air classifier guide vane improvement and inner flow field numerical simulation. *Powder Technol.* **2012**, *226*, 10–15. [CrossRef]
27. Liu, R.; Liu, J.; Yu, Y. Effects of axial inclined guide vanes on a turbo air classifier. *Powder Technol.* **2015**, *280*, 1–9. [CrossRef]
28. Yu, Y.; Chen, W.; Kong, X.; Ren, C.; Liu, J. Design of the new guide vane for the turbo air classifier. *Mater. Sci. Eng. Technol.* **2023**, *54*, 196–206. [CrossRef]
29. Bauder, A.; Müller, F.; Polke, R. Investigations concerning the separation mechanism in deflector wheel classifiers. *Int. J. Miner. Process.* **2004**, *74*, S147–S154. [CrossRef]
30. Ren, W.; Liu, J.; Yu, Y. Design of a rotor cage with non-radial arc blades for turbo air classifiers. *Powder Technol.* **2016**, *292*, 46–53. [CrossRef]
31. Zhao, H.; Liu, J.; Yu, Y. Effects of the impeller blade geometry on the performance of a turbo pneumatic separator. *Chem. Eng. Commun.* **2018**, *205*, 1641–1652. [CrossRef]
32. Mou, X.; Jia, F.; Fang, Y.; Chen, C. CFD-Based Structural Optimization of Rotor Cage for High-Efficiency Rotor Classifier. *Processes* **2021**, *9*, 1148. [CrossRef]
33. Yu, Y.; Kong, X.; Liu, J. Effect of rotor cage's outer and inner radii on the inner flow field of the turbo air classifier. *Mater. Sci. Eng. Technol.* **2020**, *51*, 908–919. [CrossRef]
34. Spötter, C.; Legenhausen, K.; Weber, A.P. Separation Characteristics of a Deflector Wheel Classifier in Stationary Conditions and at High Loadings: New Insights by Flow Visualization. *KONA* **2018**, *35*, 172–185. [CrossRef]
35. Rumpf, H. *Über die Sichtwirkung von ebenen spiraligen Luftströmungen*; TH Karlsruhe: Karlsruhe, Germany, 1939.
36. Bauer, U. *Zur trennscharfen Feinstsichtung in Fliehkraft-Abweiseradsichtern. Doctoral Thesis, Technical University of Clausthal, Clausthal-Zellerfeld, Germany, 2002*; Shaker: Aachen, Germany, 2003.
37. Leschonski, K. *IFPRI-Report on Classification of Particles in Gases*; Verf: Clausthal-Zellerfeld, Germany, 1981.
38. Schubert, H. *Handbuch der Mechanischen Verfahrenstechnik: Partikeleigenschaften, Mikroprozesse, Makroprozesse, Zerteilen, Agglomerieren, Trennen, Mischen, Schüttgut*; Wiley-VCH: Weinheim, Germany, 2003.
39. Menter, F.R. Two-equation eddy-viscosity turbulence models for engineering applications. *AIAA J.* **1994**, *32*, 1598–1605. [CrossRef]
40. Zhang, Z.; Chen, Q. Comparison of the Eulerian and Lagrangian methods for predicting particle transport in enclosed spaces. *Atmos. Environ.* **2007**, *41*, 5236–5248. [CrossRef]
41. Guizani, R.; Mokni, I.; Mhiri, H.; Bournot, P. CFD modeling and analysis of the fish-hook effect on the rotor separator's efficiency. *Powder Technol.* **2014**, *264*, 149–157. [CrossRef]
42. Eswaraiah, C.; Angadi, S.I.; Mishra, B.K. Mechanism of particle separation and analysis of fish-hook phenomenon in a circulating air classifier. *Powder Technol.* **2012**, *218*, 57–63. [CrossRef]
43. Betz, M.; Nirschl, H.; Gleiss, M. Development of a New Solver to Model the Fish-Hook Effect in a Centrifugal Classifier. *Minerals* **2021**, *11*, 663. [CrossRef]
44. Legenhausen, K. Untersuchung der Strömungsverhältnisse in Einem Abweiseradsichter. Doctoral Thesis, Technical University of Clausthal, Clausthal-Zellerfeld, Germany, 1991.
45. Galk, J. *Feinsttrennung in Abweiseradsichtern. Doctoral Thesis, Technical University of Clausthal, Clausthal-Zellerfeld, Germany, 1995*; Botermann und Botermann: Köln, Germany, 1996.
46. Németh, E. Triboelektrische Aufladung von Kunststoffen. Doctoral Thesis, TU Bergakademie Freiberg, Freiberg, Germany, 2003; Freiberg, Germany, 2004.
47. Zou, H.; Guo, L.; Xue, H.; Zhang, Y.; Shen, X.; Liu, X.; Wang, P.; He, X.; Dai, G.; Jiang, P.; et al. Quantifying and understanding the triboelectric series of inorganic non-metallic materials. *Nat. Commun.* **2020**, *11*, 2093. [CrossRef]
48. Ose, S. *Characterisation of the Bipolar Electrostatic Charging of Powders*; University of Southampton: Southampton, UK, 2001.
49. Grosshans, H.; Papalexandris, M.V. Direct numerical simulation of triboelectric charging in particle-laden turbulent channel flows. *J. Fluid Mech.* **2017**, *818*, 465–491. [CrossRef]
50. Matsusaka, S.; Masuda, H. Electrostatics of particles. *Adv. Powder Technol.* **2003**, *14*, 143–166. [CrossRef]

51. Münster, F.H. Austrittsarbeit (Work Function Table). Available online: https://www.fh-muenster.de/ciw/downloads/personal/juestel/juestel/chemie/Austrittsarbeit.pdf (accessed on 10 June 2024).
52. Mirkowska, M.; Kratzer, M.; Teichert, C.; Flachberger, H. Principal Factors of Contact Charging of Minerals for a Successful Triboelectrostatic Separation Process–a Review. *Berg. Huettenmaenn Monatsh* **2016**, *161*, 359–382. [CrossRef]
53. Hansen, L.; Weers, M.; Wollmann, A.; Weber, A.P. Forced triboelectrification of fine powders in particle wall collisions. *Minerals* **2022**, *12*, 132. [CrossRef]
54. DEKATI-ELPI+®. Available online: https://dekati.com/products/elpi/ (accessed on 11 November 2024).
55. Blazek, J. *Computational Fluid Dynamics: Principles and Applications*, 2nd ed.; Elsevier Science & Technology: Oxford, UK, 2005.